processes

MDPI

Article

Comparison of Cavitation in Two Axial-Flow Water Jet Propulsion Pumps

Zipeng Xu and Huanxin Lai *

School of Mechanical and Power Engineering, East China University of Science and Technology, Shanghai 200237, China; xuzipengd@163.com
* Correspondence: hlai@ecust.edu.cn

Abstract: To investigate the appropriate design method of the water jet pump, numerical simulations are carried out to compare the cavitation in two pumps designed by the streamline method and the blade load method. Based on a brief description of the design methods, the internal flow fields and cavitation in the two axial flow water jet propulsion pumps are studied by using the SST $k-\omega$ turbulence model and barotropic law cavitation model. The cavitation location, disturbance velocity field, blade load, and their variations with the cavitation number are analyzed. The results show that the pump designed by the blade load method has a smaller cavitation bubble than the pump designed by the streamline method. With the decrease of cavitation number, the vapor bubbles first appear at the blade tip of the leading edge and then extend from the leading edge to the trailing edge. The bubble thickness and the area of the low pressure on the suction surface also increases. A whirl in the disturbance velocity is observed, which turns the direction of incoming flow to the cavitation area. Furthermore, the head drop of water jet pump is related to the decrease of blade load. The results also show that at the point of cavitation number equal to 0.319, an unexpected peak of head in the pump designed by the streamline method is observed, which indicates an unstable working point for the pump. If the priorities are anti-cavitation performance and high efficiency at the design condition, the blade load method is the first choice to design pumps. While the streamline method should be adopted if high efficiency at large flow rates is preferred.

Keywords: water jet propulsion pump; streamline method; blade load method; cavitation flow; numerical simulation

check for updates

Citation: Xu, Z.; Lai, H. Comparison of Cavitation in Two Axial-Flow Water Jet Propulsion Pumps. *Processes* **2023**, *11*, 2137. https://doi.org/10.3390/pr11072137

Academic Editor: Weizhong Dai

Received: 19 May 2023
Revised: 13 July 2023
Accepted: 14 July 2023
Published: 17 July 2023

Copyright: © 2023 by the authors. Licensee MDPI, Basel, Switzerland. This article is an open access article distributed under the terms and conditions of the Creative Commons Attribution (CC BY) license (https://creativecommons.org/licenses/by/4.0/).

1. Introduction

Axial flow water jet propulsion pumps have the advantages of a large flow rate and high efficiency [1–3]. The maneuverability of an axial flow water jet pump for propulsion is also generally higher than that of a traditional propeller [4,5], so it is widely used in marine engineering and military applications [6]. Cavitation flow in water jet propulsion pumps is the primary source of noise, which is the critical factor affecting the submarine's stealth performance [7]. For this reason, the suppression of cavitation is a key task for the design of water jet propulsion pumps.

The design methods and the structure selection are crucial factors in the cavitation of the water jet propulsion pumps. The streamline method (SLM) and the blade load method (BLM) are two widely utilized design methods for propulsion pumps. The axial flow pumps designed by the SLM [8] have high efficiency and a broad working range. On the other hand, the BLM [9] can be employed to suppress the flow separation in the pumps by adjusting the blade load distribution. Wang et al. [8] designed an axial pump based on the SLM, and the impact of design parameters on hydraulic performance was studied. Bonaiuti et al. [10] designed a mixed flow water jet pump based on the BLM; the effect of design configurations on the hydrodynamic and suction performance was investigated. Zhou [11] applied the BLM to construct a pump-jet model. He found that

the pump designed by the BLM had high efficiency and thrust. The two methods have been used to design excellent pumps and provide options for the design of the propulsion pumps, considering the high requirements of suppressing the cavitation in the water jet propulsion pumps in the submarines, as mentioned above. Therefore, the motivation of our work is to compare the cavitation in water jet pumps designed by the two methods and provide a reference for the selection of design methods for pump designers.

In recent years, numerical simulations and experiments have been conducted to investigate the cavitation flow in axial flow water jet propulsion pumps. In an experimental study, Tan et al. [12] investigated the large scale cavitating vortical structures in the performance breakdown of an axial waterjet pump with high speed imaging and casing pressure measurements. The result showed that the perpendicular cavitating vortices led to a reduction in the flow rate and blade work in the tip region as the cavitation number decreased. As a result, the head fell rapidly. Chen et al. [13] examined the mechanisms of cavitation breakdown in an axial water jet pump. The study showed that cavitation breakdown was associated with a rapid expansion of the attached cavitation on the blade suction side into the blade overlap region. Shen et al. [14] investigated the tip leakage vortex cavitation at multi-operating conditions in an axial flow pump based on high speed photography. The results showed that the size and strength of the suction side perpendicular cavitating vortices grew with the decrease of pressure, resulting in the degradation in pump's performance. Furukawa et al. [15] investigated the blade row's interaction between the front and rear rotors of an axial flow pump. The result showed that the pressure fluctuation in the front rotor was bigger than that in the rear stator.

Because of the long period and the high expense of experimental study, numerical simulation has become an efficient method for investigating cavitation flows. Shen et al. [16] analyzed the influence of tip clearance on the flow field in an axial flow pump. The results showed that the tip leakage and the pressure fluctuation at the blade tip became severe as the tip clearance was increased. Guo et al. [17] found that the cavitation near the blade tip increased the pressure fluctuations in the flow field. Xu et al. [18] studied the interaction of cavitation and vortex in the tip region. Cao et al. [19] discussed the role of the non-uniform suction flow in the performance of water jet pump. Non-uniform suction flow was found to trigger a sharp descending of blade load, leading to a drop of the pump head. Al-Obaidi and Alhamid [20] explored the performance characteristics under five operating conditions and three blade angles in an axial flow pump. The results showed that the flow stability of pump deteriorated as the flow rates decreased, and the flow unsteadiness and pressure pulsation increased with an increase in blade angle. Al-Obaidi [21] investigated the impact of stator on the performance and flow field of an axial flow pump. The pressure, kinetic energy, and velocity were increased by adding a stator to the pump. Miorini et al. [22] analyzed the tip leakage vortex in an axial waterjet pump. The tip leakage vortex was first observed at the suction side of the blade, then migrated toward the pressure side of the neighboring blade. The migration of tip leakage vortex led to massive vortex breakdown. These investigations were focused on the effects of the blade geometrical parameters, tip leakage vortex, the impact of stator, and non-uniform flow on the performance of axial flow pumps. Cavitation at the blade tip was observed, which provided an understanding of the three-dimensional cavitation flow phenomena in the water jet propulsion pumps.

Because a submarine may operate at different depths, the pressure of the water jet propulsion pumps varies within a wide range, and the conditions are different from those traditional pumps which operate at a fixed position. The cavitation caused by the variable working conditions is particularly important. So far, there are only limited studies on the cavitation in axial flow pumps working at different depths. The understanding of such flows is relatively lacking, which is undoubtedly not helpful to the development of high-performance water jet propulsion pumps.

To investigate the appropriate design method of the water jet pump and provide some insights into the cavitation flows, numerical simulations are carried out to compare the cavitation in two pumps designed by the SLM and the BLM, respectively. The internal flow

fields and cavitation in the two pumps are given attention. An experimental study to check the design and the numerical simulations is our future work.

The remaining sections of this paper are organized as follows: The description of the design method is presented in Section 2. The equations for the cavitation flow are listed in Section 3. The numerical setup is described in Section 4. The cavitation in two pumps designed by the streamline method and the blade load method is compared in Section 5, followed by conclusions in Section 6.

2. The Design Method

2.1. Design Parameters

The design objectives of the water jet pumps are listed in Table 1. According to the relationship between the specific speed and the number of blades, 3 and 5 blades are selected for the rotor and the stator, respectively. The radius of the shroud and hub is chosen based on the correlation between the hub ratio and the specific speed. The axial chord length of the rotor and stator is determined by the connection between the cascade solidity and the blade number. A detailed description of the selection of the geometrical parameters is given in Guan [23].

Table 1. Design objectives of water jet propulsion pump.

Design Objectives	Value
Flow rate Q ($m^3 \cdot s^{-1}$)	0.15
Head H (m)	2.6
Efficiency η (%)	85
Specific speed N_s	1001

2.2. The Streamline Method

The flowchart of the SLM is shown in Figure 1a. The initial blade can be obtained by the design parameters, then numerical simulation and experiment are carried out to analyze the flow field and check whether or not the blade meets the design objective. If the design objective is not reached, the design parameters need to be re-selected, and the blade is redesigned until the design objective is met. The SLM is dependent on the design experience of engineers, and the pump designed by the method needs to be checked repeatedly. The circulation distribution from the hub to the tip is initially calculated based on the free vortex in Equation (1),

$$V_u r = \text{const} \tag{1}$$

where V_u is the circumferential component of velocity and r is the radius. Considering the viscosity of flow and the rotation of the impeller, V_u at the hub may be increased because the hub rotates with the rotor. Meanwhile, V_u at the blade tip may be decreased due to the tip clearance. Therefore, a correction coefficient ε is introduced [23] to correct V_u, as listed in Equation (2)

$$V_{u2} = \varepsilon V'_{u2} \tag{2}$$

where V_{u2} is the corrected circumferential velocity, V'_{u2} is the counterpart of V_{u2} in Equation (1), and ε is a correction coefficient whose value is between 0.9 and 1. The profile of ε is shown in Figure 2.

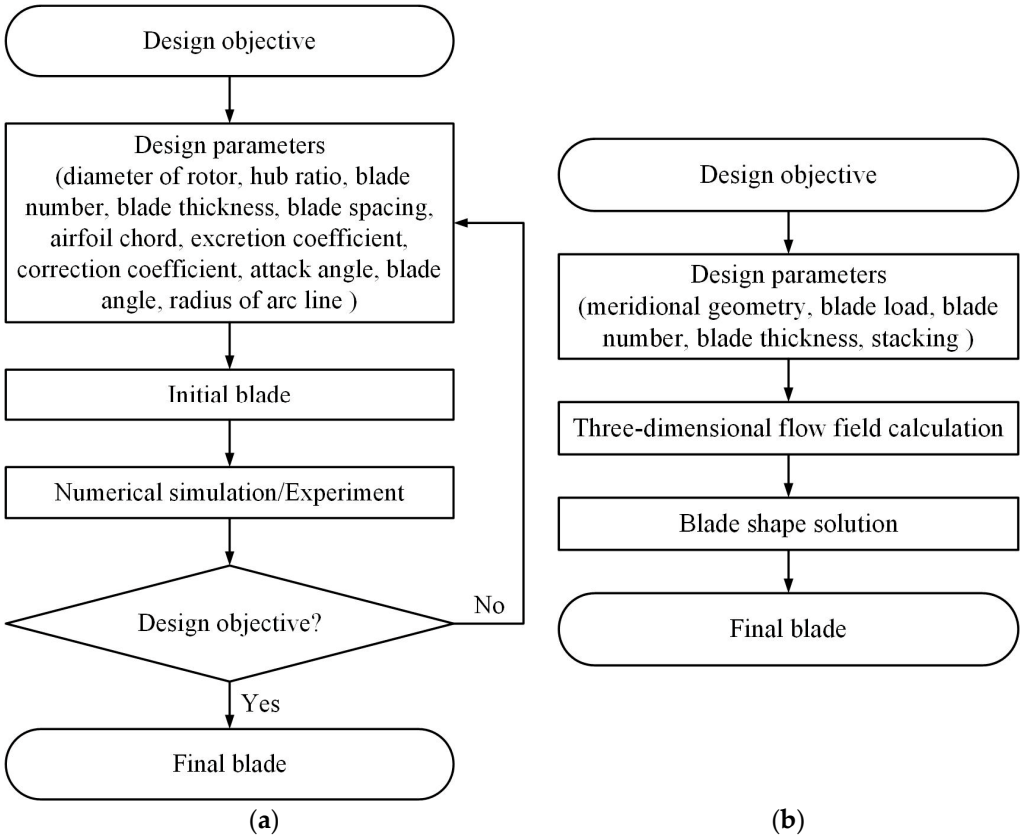


Figure 1. The flowchart of design methods (**a**) SLM and (**b**) BLM.

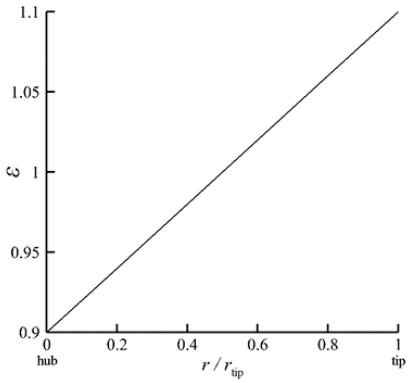


Figure 2. Spanwise distribution of correction factor.

2.3. The Blade Load Method

The BLM is an iterative solution between direct and inverse procedures. It contains flow field calculation and solution of blade geometry. The flowchart of the BLM is shown in Figure 1b. The design parameters, such as blade load, have a direct influence on the performance of the pump. Three-dimensional flow field can be obtained from the design parameters. The blade shape is described by the inverse design algorithm to meet the distribution of the flow field.

The calculation of the flow field based on the meridional geometry and the blade load distribution is a direct problem-solving step, in which the three-dimensional flow field is solved by decoupling the velocity field into a circumferentially averaged and periodic flow. The governing equations of the flow fields are presented in Equations (3) and (4),

$$\frac{\partial}{\partial r}\left(\frac{1}{r}\frac{\partial \psi}{\partial r}\right)+\frac{1}{r}\frac{\partial^2 \psi}{\partial z^2}=\frac{\partial r\overline{V}_\theta}{\partial z}\frac{\partial f}{\partial r}-\frac{\partial r\overline{V}_\theta}{\partial r}\frac{\partial f}{\partial r} \tag{3}$$

$$\frac{\partial^2 \phi_n}{\partial r^2}+\frac{1}{r}\frac{\partial \phi_n}{\partial r}+\frac{\partial^2 \phi_n}{\partial z^2}-\frac{n^2B^2}{r^2}\phi_n=\frac{e^{-inBf}}{inB}\nabla^2 r\overline{V}_\theta-e^{-inBf}\left(\frac{\partial r\overline{V}_\theta}{\partial r}\bullet\frac{\partial f}{\partial r}+\frac{\partial r\overline{V}_\theta}{\partial z}\bullet\frac{\partial f}{\partial z}\right) \tag{4}$$

where z is the axial coordinate, ψ is the stream function, $\overline{V}_\theta$ is circumferential average tangential velocity, f is the wrap angle, ϕ_n is the potential function, B is the blade number, n is the number of Fourier expansion terms, and i is the unit of an imaginary number.

The solution of blade geometry is considered the inverse problem. Assuming the relative velocity is tangent to the blade surface, the governing equation for the blade profile is obtained in Equation (5):

$$(\overline{V}_z+v_{zb1})\frac{\partial f}{\partial z}+(\overline{V}_r+v_{rb1})\frac{\partial f}{\partial r}=\frac{r\overline{V}_\theta}{r^2}+\frac{v_{\theta b1}}{r}-\omega \tag{5}$$

where $\overline{V}_z$ and $\overline{V}_r$ are the axial and radial components of the circumferential average velocity, respectively. v_{zb1}, v_{rb1}, and $v_{\theta b1}$ are the axial, radial, and tangential components of the circumferential periodic velocity, respectively. ω is the angular speed of rotation.

The BLM has fewer design parameters compared to SLM, as presented in Figure 1. The design cycle can be shorter, and less experience is needed for the designer, as compared with the traditional design methods such as SLM. So, BLM is widely used in the design of rotating machinery.

The meridional geometry, blade number, and blade thickness are specified to design the pump in the BLM. In order to compare the two design methods, these parameters for the designation using BLM are selected refer to the propulsion pump designed by the SLM. According to the recommendation by Bonaiuti et al. [10], the blade load distributions for airfoils at the hub and the tip of the blades are adjusted so as to suppress cavitation and flow separation.

3. Equations for Cavitation Flow

3.1. Governing Equations

The gas–liquid two phase flow is described by a single fluid in this paper. The liquid in the mixed phase shares the same velocity and pressure as the gas. The conservation laws of mass and momentum in the mixed phase are given in Equations (6) and (7), respectively.

$$\frac{\partial}{\partial x_j}\left(\rho_m u_j\right)=0 \tag{6}$$

$$\frac{\partial}{\partial x_j}\left(\rho_m u_i u_j\right)=-\frac{\partial p}{\partial x_i}+\frac{\partial}{\partial x_j}\left[(\mu_m+\mu_t)\left(\frac{\partial u_i}{\partial x_j}+\frac{\partial u_j}{\partial x_i}-\frac{2}{3}\frac{\partial u_k}{\partial x_k}\delta_{ij}\right)\right] \tag{7}$$

where x_i, x_j, and x_k are the Cartesian coordinate components (i = 1, 2, 3, j = 1, 2, 3, k = 1, 2, 3). ρ_m, and p are the density and pressure of the mixed phase, respectively. u_i is the velocity in the i direction, u_j is the velocity in the j direction, u_k is the velocity in the k direction, μ_m and μ_t are the dynamic viscosity and viscosity coefficient of the mixed phase, respectively. δ_{ij} is the Kronecker delta.

3.2. Cavitation Model

The cavitation model based on the barotropic law [24] describes the density of liquid and gas with pressure, which can ensure the continuity of density between gas and liquid to

predict the cavitation in the axial flow pumps. The density, dynamic viscosity, and volume fraction of the mixing phase [25] are defined in Equations (8), (9), and (10), respectively.

$$\rho_m = \frac{\rho_l + \rho_v}{2} + \frac{\rho_l - \rho_v}{2} \sin\left(\frac{p - p_v}{AMIN^2}\right) \tag{8}$$

$$\mu_m = \alpha_v \mu_v + (1 - \alpha_v)\mu_l \tag{9}$$

$$\alpha_v = \frac{\rho_l - \rho_m}{\rho_l - \rho_v} \tag{10}$$

where ρ_v and ρ_l represent the density of the gas and liquid, respectively. p_v is the saturated pressure of vapor at the same temperature, p_l is the pressure of liquid, $AMIN$ is the slope of the barotropic law, μ_l and μ_v are the dynamic viscosity of liquid and vapor, respectively. α_v is the volume fraction of vapor.

4. Calculation of Cavitation in Water Jet Pumps

4.1. The Pumps

In this paper, two water jet propulsion pumps are studied. The two pumps are designed based on the streamline method and the blade load method, respectively. For the convenience of description, the two pumps are denoted as the SLM pump and the BLM pump, respectively. A three-dimensional model of the flow configuration is shown in Figure 3. It consists of four zones, i.e., the inlet extension, the rotor, the stator, and the outlet extension. The rotor and the stator in the SLM pump are designed by the streamline method, while the rotor and the stator in the BLM pump are designed by the blade load method. The inlet extension and the outlet extension are extended upstream and downstream of the blades by twice the axial chord length at the rotor hub to avoid backflows in the computational domain, which may cause difficulty in the calculation. The main geometrical parameters of the water jet propulsion pump are summarized in Table 2.

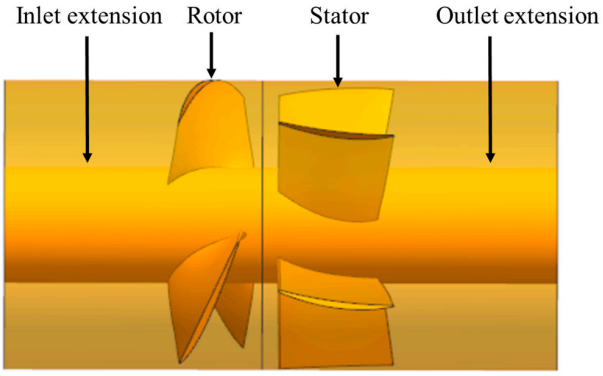


Figure 3. Three-dimensional model of the flow configuration.

Table 2. Geometrical parameters of the water jet propulsion pump.

Geometrical Parameters	Value
Blade number of the rotor	3
Blade number of the stator	5
Radius of shroud (mm)	110
Radius of hub (mm)	44
Axial chord length at rotor tip (mm)	50
Axial chord length at rotor hub (mm)	65
Axial chord length at stator tip (mm)	100
Axial chord length at stator hub (mm)	90
Inlet extension (mm)	130
Outlet extension (mm)	130
Tip clearance (mm)	0.5

The flowchart for the study process is presented in Figure 4.

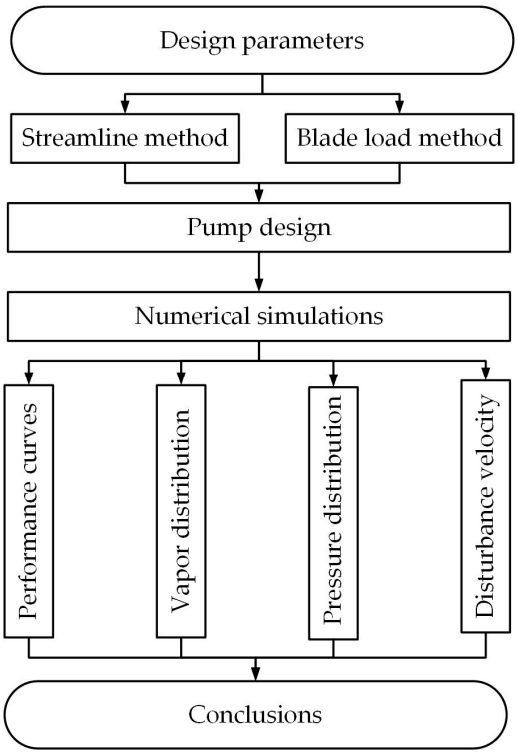


Figure 4. The flowchart for the study process.

4.2. Calculation Conditions

In the present calculations, velocity components at the inflow boundary are specified. The pressure at the outlet boundary is imposed. Cavitation flows at different depths are simulated by decreasing the pressure value at the outlet boundary, which also changes the pressure at the inlet boundary, resulting in variation of the cavitation number. A mixing plane is set up between the rotor and the stator to handle the rotor/stator problem. The hub and blades of the rotor are set as the rotating walls, where no-slip and adiabatic conditions are imposed. As the flow is subjected to the negative pressure gradient, the SST k–ω turbulence model is chosen to account for the turbulent flows [26,27]. The liquid in the calculation is water, and the temperature is 25 °C. The saturated pressure is set to 3574 Pa. The vapor density at the same temperature is 0.02308 kg/m^3, and the dynamic viscosity is 9.8626 $\times$ 10^{-6} Pa·s. The setting of boundary conditions and the selection of turbulence model for cavitating turbulent flow calculation are similar to those in Turi et al. [24], where validations are provided.

Structured grids are used for the calculation, with the H-type grids in the blade passage and the H-O grids in the blade tip clearance, as shown in Figure 5. For the convenience of description, the leading edge and the trailing edge in Figure 5 are denoted as LE and TE, respectively. The grids near the walls are stretched to capture the flow in the boundary layers. The distance between the first inner grid nodes to the wall, in terms of y+, is around 2, which meets the grid requirement of the SST $k-\omega$ turbulence model.

The calculations were based on the commercial code FINE/TURBO^{TM} developed by Numeca International. FINE/TURBO^{TM} is a three-dimensional structured mesh code that solves the time-dependent Reynolds-averaged Navier–Stokes equations. An element-based finite volume method is used in FINE/TURBO^{TM} with second-order discretization schemes in space. A second-order central difference is applied to the convection and diffusion terms.

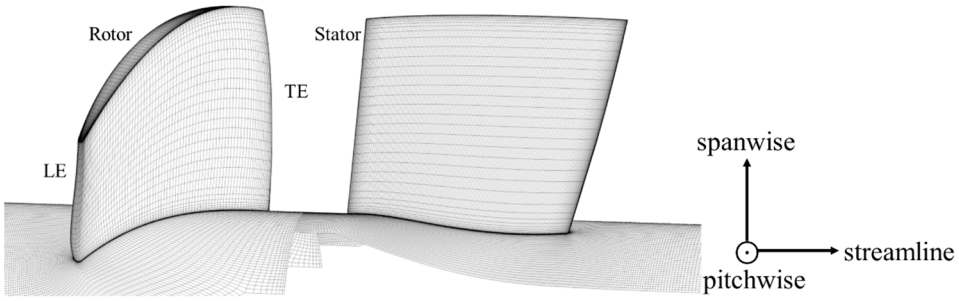


Figure 5. Structured mesh.

In order to obtain the grid-independent solution, four meshes are tested. The grid nodes in the streamwise, spanwise, and pitchwise directions for the meshes are listed in Table 3. We define the head and the efficiency in Equations (11) and (12), respectively, as follows:

$$H = \frac{P_{\text{total,out}} - P_{\text{total,in}}}{\rho_1 g} \tag{11}$$

$$\eta = \frac{\rho_1 g Q H}{M\omega} \tag{12}$$

where $P_{\text{total,in}}$ and $P_{\text{total,out}}$ are the total pressures at the inlet and outlet boundaries, respectively. g is the gravitational acceleration, Q is the flow rate at the design condition, M is the moment of the rotor.

Table 3. Meshes distribution.

Meshes	Rotor	Stator
	Streamwise × Spanwise × Pitchwise (Nodes)	
mesh I	65 × 53 × 53	61 × 33 × 25
mesh II	105 × 61 × 89	141 × 45 × 49
mesh III	129 × 71 × 105	157 × 57 × 57
Mesh IV	141 × 81 × 121	173 × 69 × 65

The head and the efficiency predicted by the four meshes for the BLM pump are plotted in Figure 6. The grids for the SLM pump are on the same level. It can be seen from Figure 6 that mesh III is fine enough to produce grid-independent results for the head and the efficiency. Their values remain constant when the mesh is further refined to mesh IV. Therefore, mesh III is employed in the following calculations.

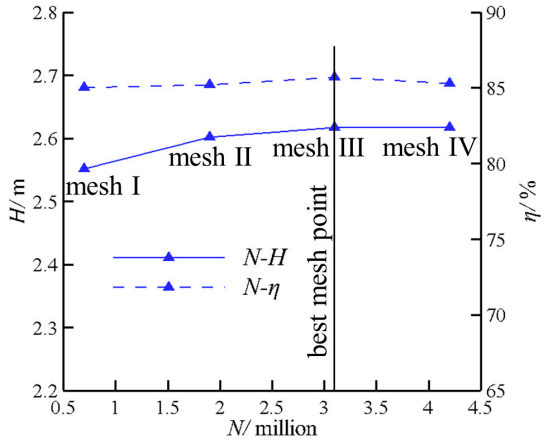


Figure 6. Grid independence check for the BLM pump.

5. Calculation of Cavitation in Water Jet Pumps

5.1. Performance Curves and Time-Averaged Flow Fields

The internal flow fields without cavitation are first analyzed. The performance curves and limiting streamlines are included. Figure 7 shows the performance curves for the two pumps, where q is the flow rate at the operating points. It can be observed from Figure 7 that the head decreases as the flow rate increases, while the efficiency increases at first and then decreases. The head and the efficiency of the SLM pump drop slower than those of the BLM pump at large flow rates, which denotes a broader working range of high efficiency for the pump.

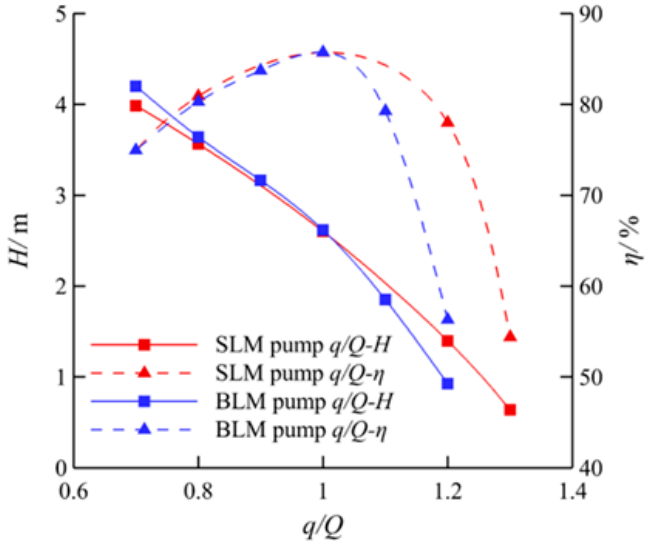


Figure 7. Performance curves of two pumps.

The limiting streamlines at the design conditions (q/Q = 1) for the two pumps are compared in Figure 8. The topology of these streamlines is quite similar for the two pumps. At the hub, a stagnation point and two reattached lines are observed near the leading edge of the pressure surface (PS), which are probably caused by the horseshoe vortices [28]. There are two separating lines near the trailing edge of the rotor's suction surface (SS) at the hub, which indicate the existence of a passage vortex. A separating line is identifiable at the rotor's suction surface near the trailing edge of the BLM pump, possibly related to the static pressure distribution from the hub to the tip [29]. The recirculation area is observed at the stator's suction surface because of the viscosity of the flow and the negative pressure gradient. The recirculation area on the stator's suction surface for the BLM pump is smaller than that of the SLM pump, which denotes smaller flow separation vortices on the stator's suction surface.

In order to investigate the cavitation flows of the propulsion pumps at different pressures, the cavitation number is defined in Equation (13):

$$\sigma = \frac{P_{\text{total,in}} - P_{\text{v}}}{\frac{1}{2}\rho_1 {u_{\text{tip}}}^2} \tag{13}$$

where $P_{\text{total,in}}$ varies due to the change of depth for the pump in water and u_{tip} is the circumferential velocity at the blade tip. The $H - \sigma$ curves for the two pumps are plotted in Figure 9. It can be seen that the heads of the pumps initially remain constant. But when the cavitation number is decreased to a specific critical value, the heads drop sharply. An unexpected peak of the head is observed at point (b) in the SLM pump. On the other hand, the $H - \sigma$ curve of the BLM pump is smoother. In order to further analyze the internal flow fields and cavitation of the propulsion pumps at different depths, the flow fields at three

cavitation number values, i.e., $\sigma = 0.492$, 0.319, and 0.246, and depicted as (a), (b), and (c) in Figure 9, respectively, are analyzed. For the point without cavitation, $\sigma = 2.224$.

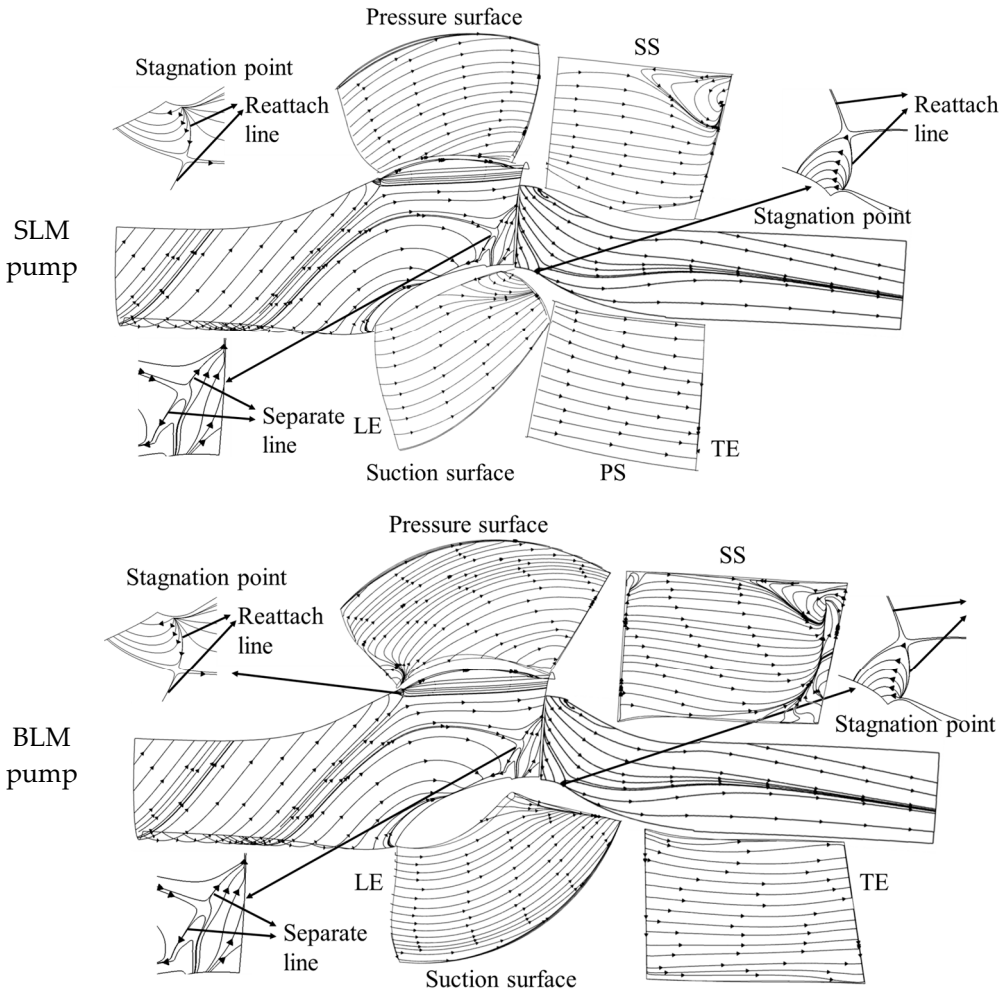


Figure 8. Distribution of limiting streamlines.

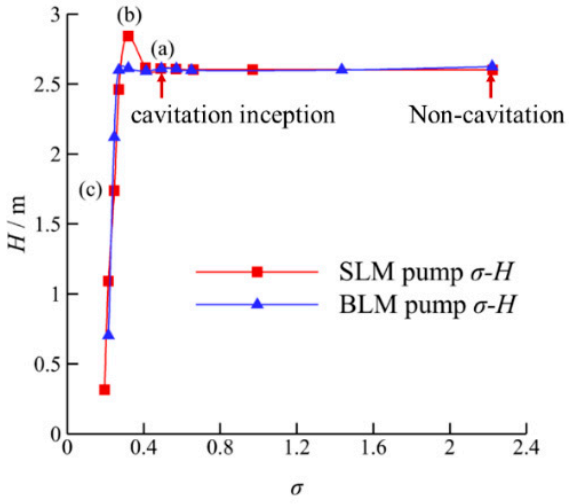


Figure 9. $H - \sigma$ curves for the two pumps (a) $\sigma = 0.492$, (b) $\sigma = 0.319$ and (c) $\sigma = 0.246$.

The variation of the blade load with cavitation numbers is investigated to analyze the peak of head at point (b). The concept of the blade load is proposed by Bonaiuti [10] in the three-dimensional inverse design, which is defined in Equation (14),

$$P^+ - P^- = \frac{2\pi}{B}\rho_l W_{\mathrm{mbl}} \frac{\partial V_\theta r}{\partial m} \tag{14}$$

where P^+ and P^- are the static pressure values on the pressure surface and the suction surface, respectively. W_{mbl} is the projection component of relative velocity, m is the dimensionless meridional distance from the leading edge to the trailing edge, and its value is between 0 and 1. $\frac{\partial V_\theta r}{\partial m}$ is called blade load. Its integration along the meridional distance is the total velocity circulation from the leading edge to the trailing edge, as presented in Equation (15), which denotes the work-doing capacity of the blade. The relationship between the pump's head and the velocity circulation [23] is presented in Equation (16). The angular speed of rotation ω is constant, so the pump's head is proportional to the velocity circulation. The dimensionless distance between the hub and the tip, S, is defined in Equation (17):

$$\int_0^1 \frac{\partial V_\theta r}{\partial m} dm = V_\theta r \tag{15}$$

$$H = \frac{\omega r V_\theta}{g} \tag{16}$$

$$S = \frac{r - r_{\mathrm{hub}}}{r_{\mathrm{tip}} - r_{\mathrm{hub}}} \tag{17}$$

where r_{hub} and r_{tip} are the radiuses at the hub and the tip, respectively. The blade load distributions on the $S = 0.5$ rotary surface for the two pumps are shown in Figure 10. It can be found that the blade loads fluctuate near the leading edge. As the meridional distance increases, the blade loads increase at first and then decrease. The differences in the blade load distributions between the $\sigma = 2.224$ and the $\sigma = 0.492$ cases occur only at the leading edge, which are probably caused by the vapor at the leading edge of the suction surface. In the $\sigma = 0.319$ case, the area enclosed by the blade load and the meridional distance for the SLM pump are larger than that for the BLM pump, so the total velocity circulation in SLM pump is bigger than that for the BLM pump. That is the reason for the peak of head at point (b) in Figure 9. In the other cases ($\sigma = 0.492, 0.246$), the heads drop as the blade load decreases, which are consistent with the results in Figure 9.

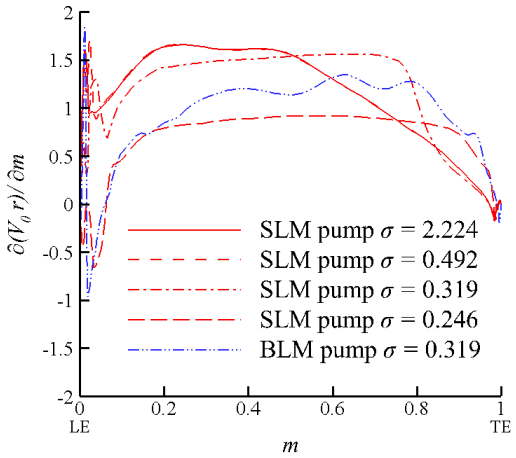


Figure 10. Blade load distributions on the $S = 0.5$ rotary surface.

The blade load with the cavitation numbers is consistent with the head drop in Figure 10. The blade loads of the two pumps initially remain constant as the cavitation number decreases from 2.224 to 0.492. As the cavitation number further decreases, the blade load of the BLM pump is decreased, while the blade load of SLM pump increases at first and then decreases.

The vapor distribution is closely relevant to the local pressure in the flow field. The static pressure coefficient is defined in Equation (18):

$$C_p = \frac{P_{static} - P_v}{\frac{1}{2}\rho_l {u_{tip}}^2} \tag{18}$$

where P_{static} is the static pressure. Figure 11 shows the distribution of pressure coefficient in the $S = 0.5$ rotary surface.

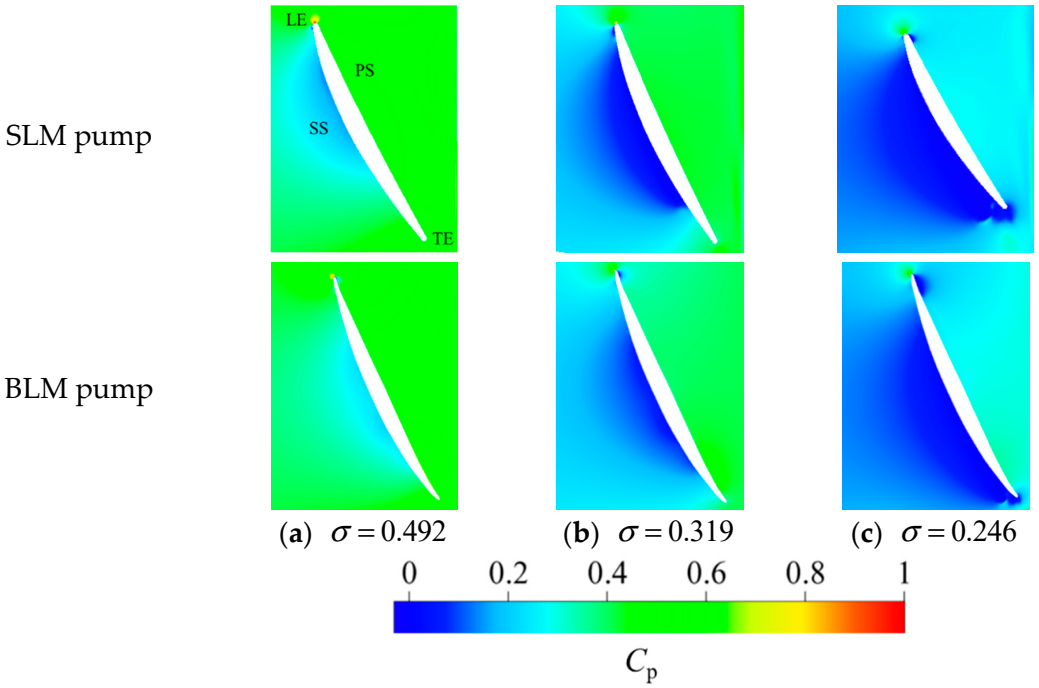


Figure 11. Pressure coefficient on the $S = 0.5$ rotary surface (**a**) $\sigma = 0.492$, (**b**) $\sigma = 0.319$ and (**c**) $\sigma = 0.246$.

The area of the low pressure on the suction surface increases while the area of the high pressure decreases with the decrease of cavitation number. The pressure of the BLM pump is higher than that of the SLM pump, which is beneficial to suppress cavitation in the pump.

5.2. Vapor Distribution

The vapor distribution on the suction surface of the rotor is shown in Figure 12. The gray area is the isosurface with vapor fraction ($\alpha_v = 0.6$). For the SLM pump, the cavitation bubbles firstly appear at the blade tip of the leading edge at the point of cavitation inception ($\sigma = 0.492$), and the head remains constant, which indicates that the cavitation is weak and has negligible impact on the pump's head. Later, the vapor expands from the leading edge to the trailing edge at the cavitation number $\sigma = 0.319$. Meanwhile, it also begins to extend from the blade tip to the hub. At this point, a peak of head is observed with the expansion of vapor, which indicates an unstable working point for the pump. When the cavitation number σ falls to 0.246, the bubble thickness increases, and the vapor covers nearly half of the suction surface. The blade's work-doing capacity is reduced, with a sharp deterioration in the pump's head. The BLM pump has a smaller cavitation bubble than the SLM pump.

In the $\sigma = 0.492$ and 0.319 cases for the BLM pump, no bubble is found in the leading edge and the blade tip. As the cavitation number decreases to 0.246, the vapor bubbles begin to appear at the blade's trailing edge, which decreases the pump's head. The cavitation distribution described above agrees with the head drop curve shown in Figure 9.

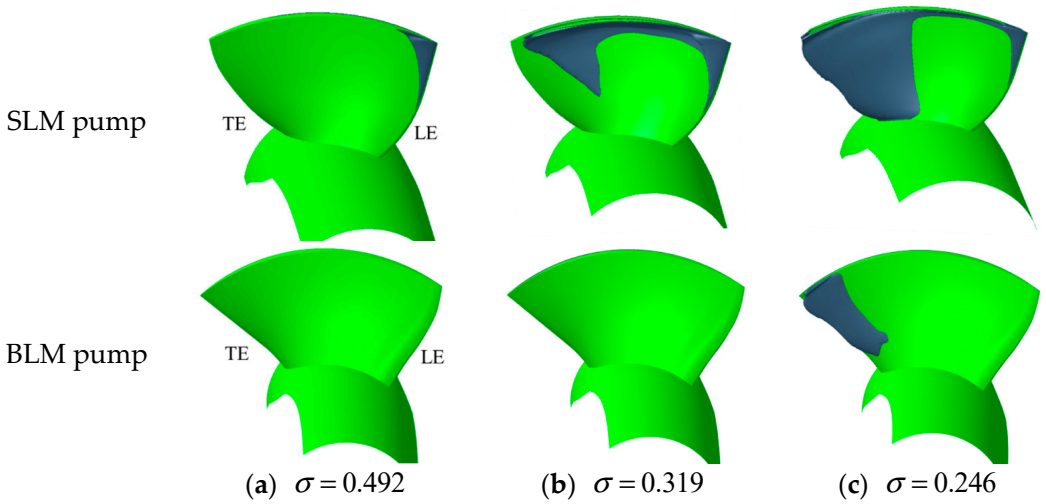


Figure 12. Vapor distribution on the suction surface of the rotor (**a**) $\sigma = 0.492$, (**b**) $\sigma = 0.319$ and (**c**) $\sigma = 0.246$.

The difference in the effect of cavitation on the head curves of the two pumps is in the 0.319 case. The cavitation on the rotor's suction surface in the SLM pump leads to the increase in the blade load, so a peak of head is observed. While cavitation has not occurred in the BLM pump, the head remains constant.

Shown in Figure 13 is the spanwise distribution of vapor, where water is depicted by the color with $\alpha_v = 0$ while the bubbles are shown by the color with $\alpha_v > 0$. The vapor distribution on the rotary surface $S = 0.5$ is shown in the red box. It can be seen from Figure 13 that the cavitation bubble size is increased as the cavitation number decreases. For the SLM pump, no visible cavitation bubble is observed in the vicinity of the blade at $\sigma = 0.492$. As the cavitation number decreases, the vapor on the suction surface of the blade expands from the leading edge to the trailing edge. At $\sigma = 0.246$, the cavitation on the suction surface expands further, and the vapor starts to appear at the leading edge of the pressure surface, as shown in Figure 13c.

For the BLM pump, only small vapors appear on the leading edge of the pressure surface in the $\sigma = 0.492$ and 0.319 cases. When the cavitation number is decreased to 0.246, the vapor appears on the suction surface near the trailing edge, and the vapor on the pressure surface gradually extends. The distribution of vapor described above agrees with the distribution of the low pressure area in Figure 11. In the spanwise direction, cavitation is more likely to occur due to the high velocity as spanwise increases. The BLM pump has a smaller cavitation bubble than the SLM pump on the same rotary surface.

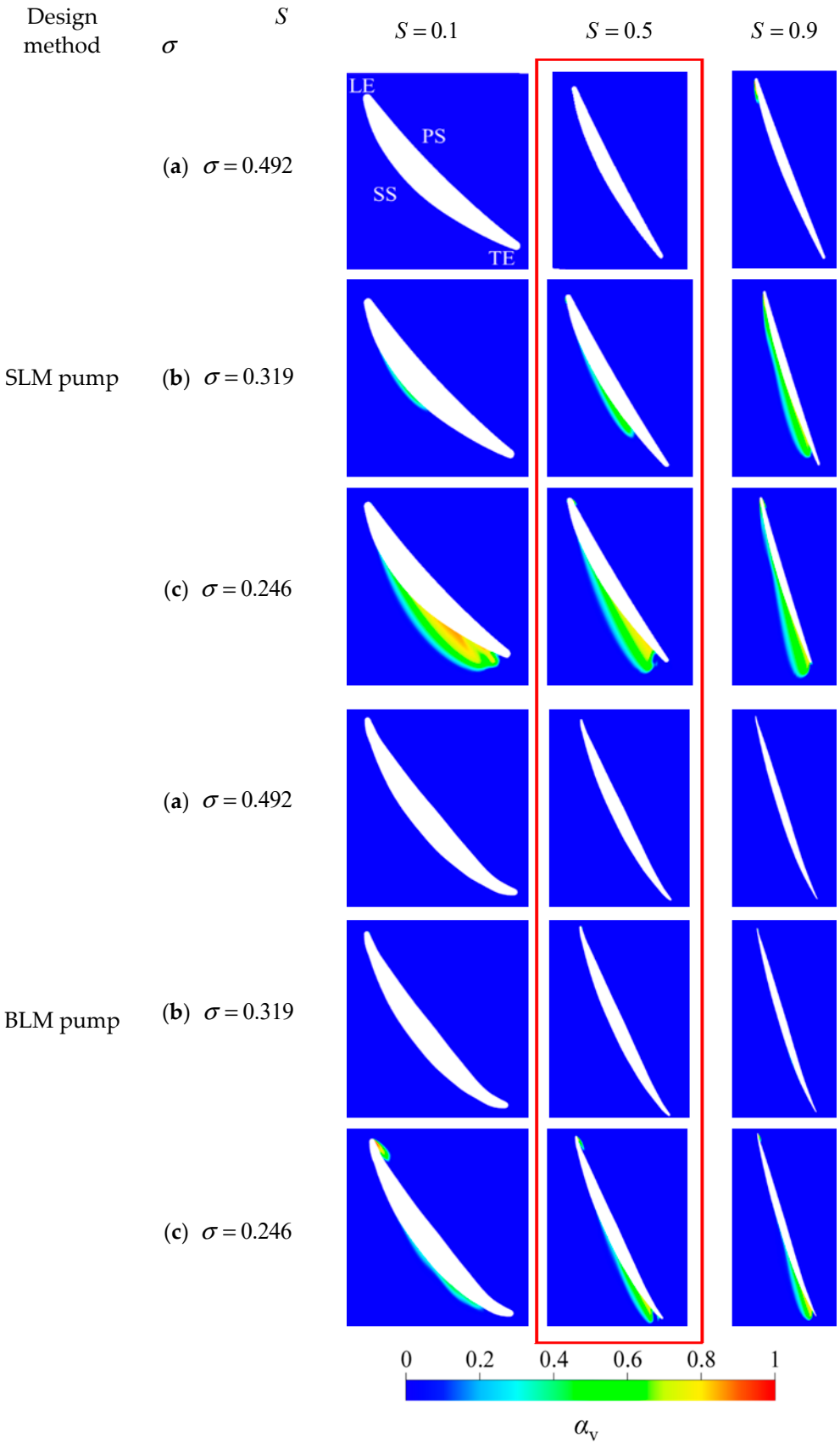


Figure 13. Spanwise distribution of vapor (**a**) $\sigma = 0.492$, (**b**) $\sigma = 0.319$ and (**c**) $\sigma = 0.246$.

5.3. Disturbance Velocity

The disturbance velocity is calculated by subtracting the velocity vector without cavitation (at $\sigma = 2.224$) from that under the cavitation conditions [30]. It can be used to clarify the effect of cavitation on the velocity in the flow field. The disturbance velocity vectors on the $S = 0.5$ rotary surface are shown in Figure 14, where the white arrows denote the direction of the disturbance velocity.

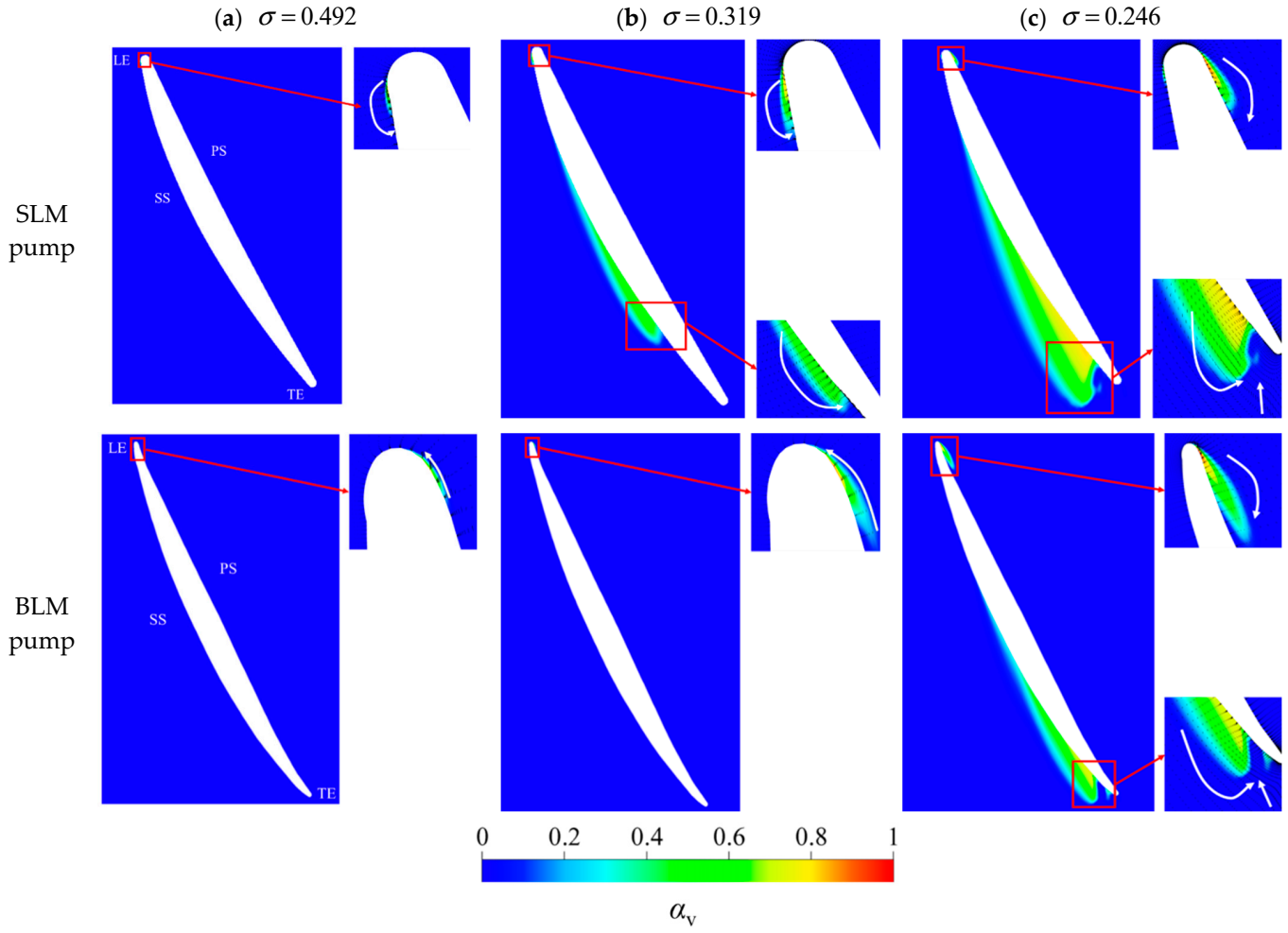


Figure 14. Disturbance velocity on the $S = 0.5$ rotary surface (**a**) $\sigma = 0.492$, (**b**) $\sigma = 0.319$ and (**c**) $\sigma = 0.246$.

It can be noticed that the disturbance velocities at each cavitation number for the two pumps are different. For the SLM pump, a whirl in the disturbance velocity field is observed at the leading edge of the suction side in the $\sigma = 0.492$ case. The whirl turns the direction of incoming flow to the cavitation area. As the cavitation number decreases, the whirl migrates gradually to the trailing edge of the suction side with the expansion of the bubbles. When the cavitation number is decreased to 0.246, the whirl at the leading edge is transferred from the suction side to the pressure side. For the BLM pump, the whirl is also observed in the flow fields.

6. Conclusions

In this paper, numerical simulations are carried out to compare the cavitation in two pumps designed by the SLM and the BLM, respectively. Attention is paid to the changes of internal flow fields with the variation of the cavitation number. The main conclusions are summarized as follows:

1. The BLM pump has a smaller cavitation bubble than the SLM pump under cavitation conditions, while the SLM pump has a slightly wider working range of high efficiency without cavitation conditions.
2. The cavitation bubbles first appear at the blade tip of the leading edge, then extend from the leading edge to the trailing edge. The area of low pressure and the bubble thickness on the suction side increase as the cavitation number decreases.
3. Under cavitation conditions, the head curves of the two pumps initially remain constant. But when the cavitation number is decreased to a specific critical value, the head curves drop sharply.
4. If the priorities are anti-cavitation performance and high efficiency at the design condition, the BLM is the first choice to design pumps, while the SLM should be adopted if high efficiency at large flow rates is preferred.

Axial water jet propulsion pump is a new technology for submarine engineering. There are quite a lot of issues which are not fully investigated, such as the tip leakage vortex on the cavitation and noise, the interactions between blade rows, and the high fidelity experimental data of the flow fields, to name a few. These questions are also possible further work for researchers in the related disciplines.

Author Contributions: Conceptualization, H.L.; Numerical calculations, Z.X.; Data analysis, Z.X.; Funding acquisition, H.L.; Writing—original draft preparation, Z.X.; Writing—review and editing, H.L.; Resources, H.L. All authors have read and agreed to the published version of the manuscript.

Funding: This work is financially supported by the National Key Research and Development Program of China [2018YFA0704604]. Thanks are also given to the Funding by the National Natural Science Foundation of China under Grant 51976061.

Data Availability Statement: All relevant data are presented in the article.

Conflicts of Interest: The authors declare no conflict of interest.

References

1. Nguyen, D.A.; Ma, S.B.; Kim, S.; Kim, J.H. Influence of inflow directions and setting angle of inlet guide vane on hydraulic performance of an axial-flow pump. *Sci. Rep.* **2023**, *13*, 22. [CrossRef]
2. Park, H.S.; Miao, F.Q.; Nguyen, T.T. Impeller design for an axial-flow pump based on multi-objective optimization. *Indian J. Eng. Mat. Sci.* **2018**, *25*, 183–190.
3. Zhang, H.; Wang, J.; Zhang, D.S.; Shi, W.D.; Zang, J.B. Numerical Analysis of the Effect of Cavitation on the Tip Leakage Vortex in an Axial-Flow Pump. *J. Mar. Sci. Eng.* **2021**, *9*, 21. [CrossRef]
4. Huang, R.F.; Wang, Y.W.; Du, T.Z.; Luo, X.W.; Zhang, W.; Dai, Y.X. Mechanism analyses of the unsteady vortical cavitation behaviors for a waterjet pump in a non-uniform inflow. *Ocean Eng.* **2021**, *233*, 14. [CrossRef]
5. Lu, Y.M.; Liu, H.R.; Wang, X.F.; Wang, H. Study of the Operating Characteristics for the High-Speed Water Jet Pump Installed on the Underwater Vehicle with Different Cruising Speeds. *J. Mar. Sci. Eng.* **2021**, *9*, 22. [CrossRef]
6. Wang, C.; Lu, L. Numerical Simulation of Propulsion Performance of a Pump-Jet Propulsor in Oblique Flow. *J. Propul. Technol.* **2020**, *41*, 2596–2604. (In Chinese) [CrossRef]
7. Jeong, S.J.; Hong, S.Y.; Song, J.H.; Kwon, H.W.; Seol, H.S. Numerical method to determine the cavitation inception speed of a submarine propeller based on the noise obtained from bubble dynamics. *Ocean Eng.* **2022**, *245*, 14. [CrossRef]
8. Wang, K.; Li, L.; Wang, Y.; Zhang, S. Design and hydraulic performance studies on an axial lead-bismuth pump for GEN-IV reactors. *Int. J. Energy Res.* **2021**, *45*, 11822–11836. [CrossRef]
9. Goto, A.; Zangeneh, M. Hydrodynamic design of pump diffuser using inverse design method and CFD. *J. Fluids Eng.-Trans. ASME* **2002**, *124*, 319–328. [CrossRef]
10. Bonaiuti, D.; Zangeneh, M.; Aartojarvi, R.; Eriksson, J. Parametric Design of a Waterjet Pump by Means of Inverse Design, CFD Calculations and Experimental Analyses. *J. Fluids Eng.-Trans. ASME* **2010**, *132*, 15. [CrossRef]
11. Zhou, Y.K.; Wang, L.Y.; Yuan, J.P.; Luo, W.; Fu, Y.X.; Chen, Y.; Wang, Z.L.; Xu, J.A.; Lu, R. Comparative Investigation on Hydrodynamic Performance of Pump-Jet Propulsion Designed by Direct and Inverse Design Methods. *Mathematics* **2021**, *9*, 343. [CrossRef]
12. Tan, D.; Li, Y.C.; Wilkes, I.; Vagnoni, E.; Miorini, R.L.; Katz, J. Experimental Investigation of the Role of Large Scale Cavitating Vortical Structures in Performance Breakdown of an Axial Waterjet Pump. *J. Fluids Eng.-Trans. ASME* **2015**, *137*, 14. [CrossRef]
13. Chen, H.; Doeller, N.; Li, Y.C.; Katz, J. Experimental Investigations of Cavitation Performance Breakdown in an Axial Waterjet Pump. *J. Fluids Eng.-Trans. ASME* **2020**, *142*, 15. [CrossRef]

14. Shen, X.; Zhang, D.S.; Xu, B.; Jin, Y.X.; Shi, W.D.; van Esch, B.P.M. Experimental Investigation of the Transient Patterns and Pressure Evolution of Tip Leakage Vortex and Induced-Vortices Cavitation in an Axial Flow Pump. *J. Fluids Eng.-Trans. ASME* **2020**, *142*, 11. [CrossRef]
15. Furukawa, A.; Takano, T.; Shigemitsu, T.; Okuma, K.; Watanabe, S. Blade rows interaction of contra-rotating axial flow pump in pressure field on casing wall. *JSME Int. J. Ser. B-Fluids Therm. Eng.* **2006**, *49*, 670–677. [CrossRef]
16. Shen, J.; Xu, F.; Cheng, L.; Pan, W.; Ge, Y.; Li, J.; Zhang, J. Simulation of internal flow characteristics of an axial flow pump with variable tip clearance. *Water* **2022**, *14*, 1652. [CrossRef]
17. Guo, Q.; Huang, X.; Qiu, B. Numerical investigation of the blade tip leakage vortex cavitation in a waterjet pump. *Ocean Eng.* **2019**, *187*, 106170. [CrossRef]
18. Xu, S.; Long, X.P.; Ji, B.; Li, G.B.; Song, T. Vortex dynamic characteristics of unsteady tip clearance cavitation in a waterjet pump determined with different vortex identification methods. *J. Mech. Sci. Technol.* **2019**, *33*, 5901–5912. [CrossRef]
19. Cao, P.Y.; Wang, Y.; Kang, C.; Li, G.D.; Zhang, X. Investigation of the role of non-uniform suction flow in the performance of water-jet pump. *Ocean Eng.* **2017**, *140*, 258–269. [CrossRef]
20. Al-Obaidi, A.R.; Alhamid, J. Investigation of the Main Flow Characteristics Mechanism and Flow Dynamics within an Axial Flow Pump Based on Different Transient Load Conditions. *Iran. J. Sci. Technol.-Trans. Mech. Eng.* **2023**, 1–19. [CrossRef]
21. Al-Obaidi, A.R. Effect of Different Guide Vane Configurations on Flow Field Investigation and Performances of an Axial Pump Based on CFD Analysis and Vibration Investigation. *Exp. Tech.* **2023**, 1–20. [CrossRef]
22. Miorini, R.L.; Wu, H.X.; Katz, J. The Internal Structure of the Tip Leakage Vortex within the Rotor of an Axial Waterjet Pump. *J. Turbomach.-Trans. ASME* **2012**, *134*, 12. [CrossRef]
23. Guan, X.F. *Morden Pumps Theory and Design*; Aerospace Publishing House: Beijing, China, 2011.
24. Turi, F.; Fortes-Patella, R.; Balarac, G. Numerical Methodology to Predict and Analyze Cavitating Flows in a Kaplan Turbine. *Int. J. Fluid Mach. Syst.* **2019**, *12*, 439–450. [CrossRef]
25. Chen, Y.; Chen, X.; Gong, Z.X.; Li, J.; Lu, C.J. Numerical investigation on the dynamic behavior of sheet/cloud cavitation regimes around hydrofoil. *Appl. Math. Model.* **2016**, *40*, 5835–5857. [CrossRef]
26. Huang, R.F.; Ji, B.; Luo, X.W.; Zhai, Z.H.; Zhou, J.J. Numerical investigation of cavitation-vortex interaction in a mixed-flow waterjet pump. *J. Mech. Sci. Technol.* **2015**, *29*, 3707–3716. [CrossRef]
27. Qiu, C.C.; Pan, G.; Huang, Q.G.; Shi, Y. Numerical analysis of unsteady hydrodynamic performance of pump-jet propulsor in oblique flow. *Int. J. Nav. Archit. Ocean Eng.* **2020**, *12*, 102–115. [CrossRef]
28. Doerffer, P.; Flaszynski, P.; Magagnato, F. Streamwise Vortex Interaction with a Horseshoe Vortex. *J. Therm. Sci.* **2003**, *12*, 304–309. [CrossRef]
29. Zangeneh, M.; Goto, A.; Harada, H. On the design criteria for suppression of secondary flows in centrifugal and mixed flow impellers. *J. Turbomach.* **1998**, *120*, 723–735. [CrossRef]
30. Kang, D.; Yonezawa, K.; Horiguchi, H.; Kawata, Y.; Tsujimoto, Y. Cause of cavitation instabilities in three dimensional inducer. *Int. J. Fluid Mach. Syst.* **2009**, *2*, 206–214. [CrossRef]

Disclaimer/Publisher's Note: The statements, opinions and data contained in all publications are solely those of the individual author(s) and contributor(s) and not of MDPI and/or the editor(s). MDPI and/or the editor(s) disclaim responsibility for any injury to people or property resulting from any ideas, methods, instructions or products referred to in the content.